Journal of Materials Research and Technology 31 (2024) 170–186

Contents lists available at ScienceDirect

Journal of Materials Research and Technology

journal homepage: www.elsevier.com/locate/jmrt

Effects of graphene addition on the mechanical, friction and corrosion properties of laser powder bed fusion 316L stainless steel

Mengqi Liu, Chaorui Jiang, Zhongxiong Kang, Xin Liu, Zhihui Zhang *, Luquan Ren

Key Lab of Bionic Engineering, Ministry of Education, Jilin University, Changchun, 130022, China

ARTICLE INFO

Handling Editor: SN Monteiro

Keywords:
LPBF-316L
Graphene composite
Corrosion resistance
Mechanical property
Friction behavior

ABSTRACT

Laser powder bed fusion of 316 L (LPBF-316 L) has been known to exhibit high ductility but low strength, along with strong corrosion resistance and weak anti-friction properties. Graphene is commonly utilized as a reinforcement phase in metals fabricated through LPBF, as this process helps reduce the tendency of graphene to agglomerate. Therefore, it is crucial to investigate the impact of incorporating graphene into the LPBF-316 L alloy, aiming to enhance toughening and anti-friction properties while maintaining the original corrosion resistance. Various concentrations of graphene were incorporated into 316 L powder and processed using LPBF. The study examined the impact of graphene concentration on the electrochemical, mechanical, and friction properties of the resulting composites. The study revealed a significant reduction in corrosion current from 8.05 $\pm$ 0.6 $\times$ 10^{-7} A/cm^2 to 6.61 $\pm$ 0.8 $\times$ 10^{-8} A/cm^2. The 15-day immersion experiment further validated that the incorporation of graphene contributed to enhancing the stability of corrosion resistance. Additionally, the presence of graphene led to improved strength and ductility in LPBF-316 L through grain refinement and precipitation. Notably, samples containing 0.2 wt% graphene exhibited a tensile fracture strength of 927.4 MPa and ductility of 54.75%. In addition, the compressive fracture strength of 2342.8 MPa, both surpassing that of LPBF-316 L. Furthermore, the study investigated the impact of graphene content on the friction of LPBF-316 L, revealing that graphene addition increased matrix hardness, reduced COF, and enhanced wear resistance. Overall, the findings suggest that graphene serves as an effective reinforcing agent for 316 L stainless steel matrix composites, enhancing mechanical properties, friction resistance, and wear resistance while preserving original corrosion resistance.

1. Introduction

Austenitic 316 L stainless steel is known for its strong intergranular corrosion resistance, good weldability, and excellent ductility, making it a popular choice in both daily life and industrial applications [1–3]. Recently, manufacturing processes have evolved to include plastic working methods for creating 316 L structures such as plates, wires, and cables. However, the increasing demand for high-strength and lightweight constructions has led to the development of more complex structures like TPMS structures, BCC lattice structures, and others. These intricate designs present a challenge for traditional preparation techniques, making it difficult to effectively handle the complexities of these structures.

In recent years, additive manufacturing (AM) has emerged as a distinct process compared to traditional subtractive fabrication methods, enabling efficient production of intricate or personalized parts [4–7]. These techniques involve building materials layer by layer in a vertical direction based on various 3D models. Among the methods used for metal fabrication, laser powder bed fusion (LPBF) stands out as a popular choice, including selective laser melting (SLM), direct laser deposition (DLD), directed energy deposition (DED), and others [8–10]. The study of LPBF-316 L has garnered attention from researchers and scholars worldwide [11]. Larimian et al. [12] conducted a study on laser processing strategies, showing that alternating laser processing enhanced the densities, mechanical properties, and microhardness of LPBF-316 L. Dutt et al. [13] found that laser processing parameters such as laser power, scanning speed, layer thickness, and hatch spacing significantly affect tensile strength, with LPBF-316 L achieving a strength of 743.1 MPa through parameter optimization. These experiments indicate that parameter-optimized LPBF-316 L exhibits superior mechanical properties compared to conventional processes due to the fine-grained metal tissue retained during the fast melting and cooling

* Corresponding author.
E-mail address: zhzh@jlu.edu.cn (Z. Zhang).

https://doi.org/10.1016/j.jmrt.2024.06.061
Received 24 March 2024; Received in revised form 1 June 2024; Accepted 9 June 2024
Available online 10 June 2024

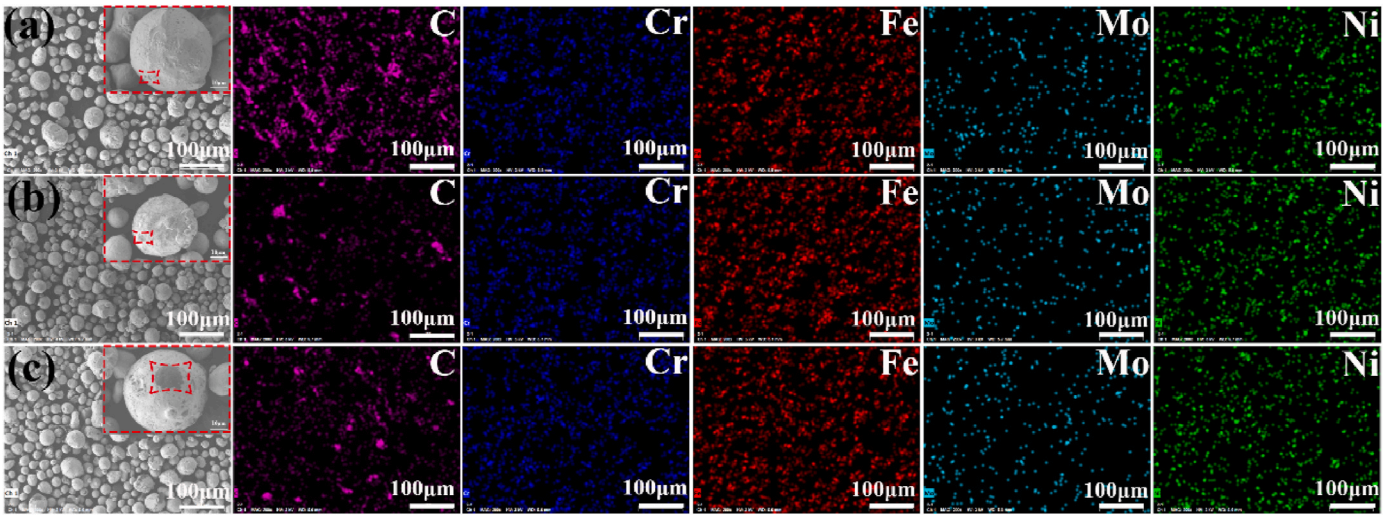

Fig. 1. SEM image of 316 L powder after mixing graphene with different contents, (a) 0.1 wt%, (b) 0.2 wt%, (c) 0.3 wt%.

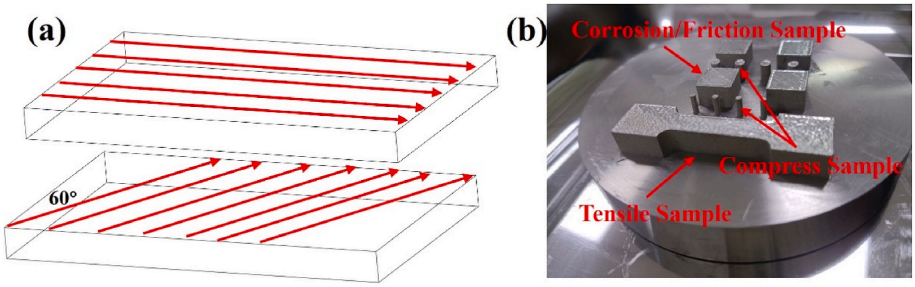

Fig. 2. (a) Scanning strategy of 316 L, (b) The 316 L samples with 0.2 wt% graphene fabricated by LPBF.

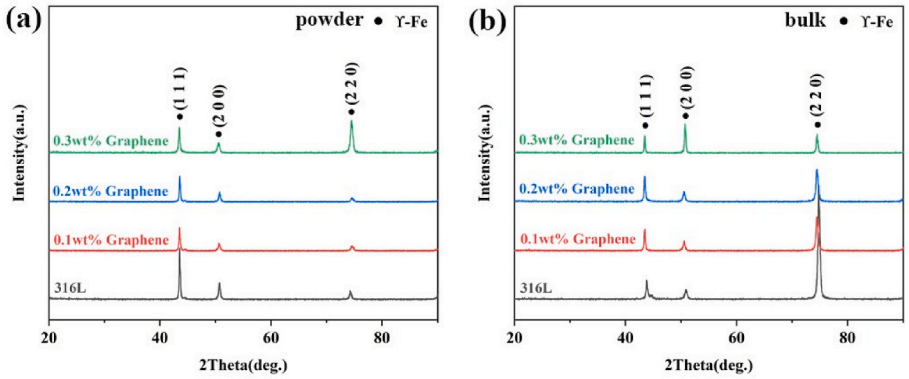

Fig. 3. XRD profiles for 316 L powders and bulks with graphene addition, (a) Powders, (b) Bulks.

processes of LPBF. Furthermore, studies by Wei et al. [14] on the lightweight and high-strength 316 L Kelvin unit lattice structure, and Rosa et al. [15] according to the amplitude dependent internal friction (ADIF) mechanism, a highly damped 316 L BCC lattice structure is produced using the additional internal friction generated by partially molten particles and spatter produced during the additive manufacturing process, highlighting the promising applications of LPBF-316 L alloy. Despite these advancements, challenges such as wear resistance and low strength persist, limiting the use of 316 L in extreme environments, reducing component service life, and increasing losses in moving mechanical parts.

The dispersion of harder and stiffer ceramic-reinforced particles into soft steel matrices has proven to be an effective method for enhancing their strength and wear resistance upon most occasions [16,17]. It is crucial to incorporate this type of hard particle reinforcing phase into LPBF processes, as the rapid cooling involved can significantly decrease the diffusion growth time of the few micro/nanoparticle reinforcing phases, resulting in a more uniform reinforcement distribution. Y_2O_3 added to LPBF-316 L was found to increase its strength due to the Orowan strengthening mechanism caused by fact that the added nanoparticles acted as barrier to dislocation movement according to Zhai et al. [18]. Similarly, the addition of TiC to 316 L, as studied by AlMangour et al. [19], Zhai et al. [20], and Li et al. [21], also demonstrated improvements in mechanical properties and friction. However, these additives primarily enhance friction resistance, with a trade-off of reduced ductility. In addition to ceramic reinforcements, graphene

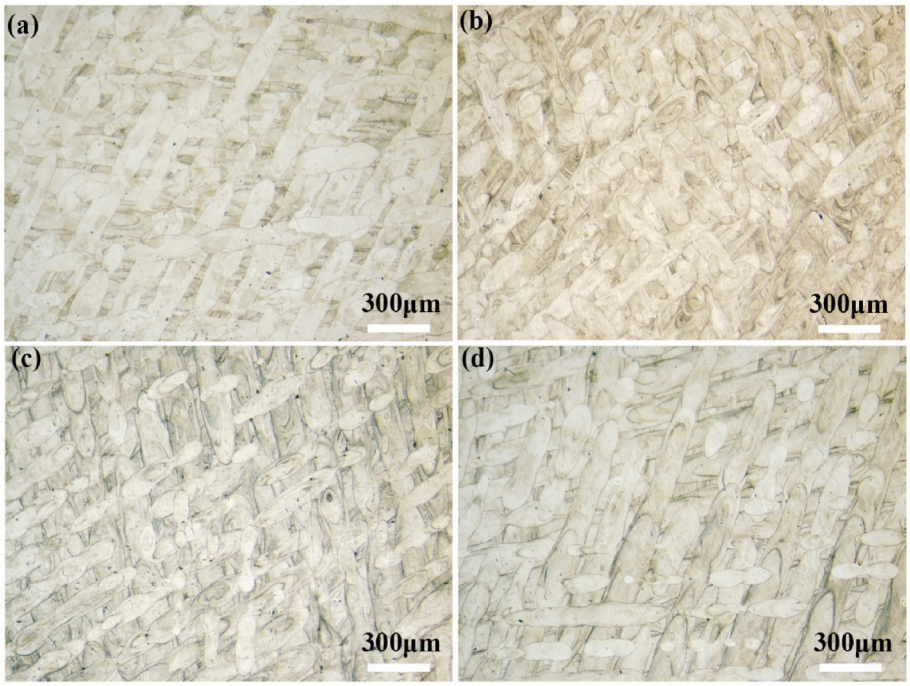

Fig. 4. Metallographic structure of 316 L powder with different graphene content, (a) LPBF-316 L, (b) 0.1 wt% graphene, (c) 0.2 wt% graphene, (d) 0.3 wt % graphene.

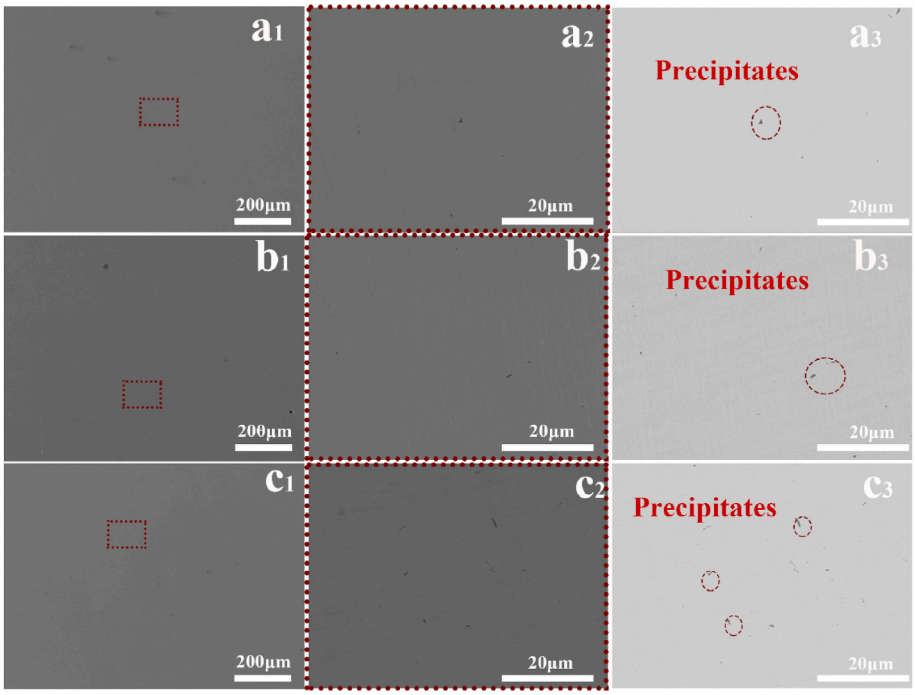

Fig. 5. SEM images showing microstructures of LPBF-316 L with graphene, (a) 0.1 wt% graphene, (b) 0.2 wt% graphene, (c) 0.3 wt% graphene.

exhibits exceptional properties in various aspects, leading to the formation of graphene-reinforced metal matrix composites that enhance mechanical and friction properties. The addition of 0.6 wt% graphene to AlSi10Mg alloys, as shown in a study by Ref. [22], resulted in a synergistic increase in both ductility and strength. In the case of LPBF-316 L, Mandal et al. [23] found that incorporating graphene enhanced hardness, reduced wear, and improved friction resistance. However, there is limited literature exploring the impact of graphene on corrosion and mechanical properties.

In this paper, the primary objective is to enhance the mechanical properties and friction resistance of LPBF-316 L while maintaining its anti-corrosion properties. This study examines the impact of different concentrations of graphene (0.1 wt%, 0.2 wt%, and 0.3 wt%) on the microstructure and phase composition of LPBF-316 L. The research includes a detailed evaluation of its anti-corrosion, frictional, and mechanical characteristics, followed by a comparative analysis for performance optimization. This approach offers a novel strategy for improving the overall performance of LPBF-316 L.

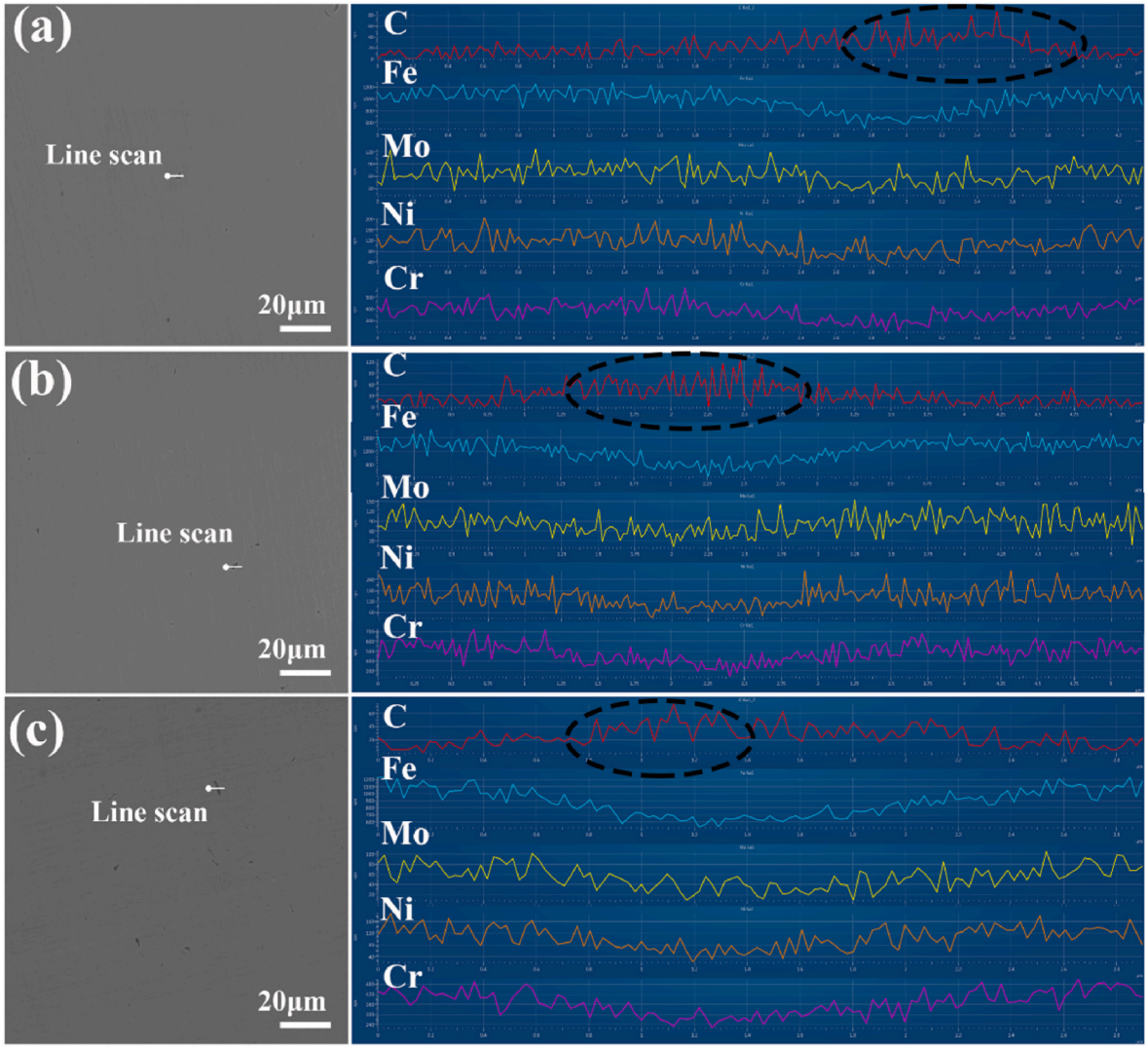

Fig. 6. Line scanning of 316 L powder with different graphene content, (a) 0.1 wt%, (b) 0.2 wt%, (c) 0.3 wt%.

2. Experimental procedures

2.1. Powder preparation and fabrication of sample

The gas-atomised spherical 316 L stainless steel powder, with particle sizes ranging from 15 to 53 μm, was combined with 0.1 wt%, 0.2 wt %, and 0.3 wt% graphene as reinforcing particles, each with a length of 0.5–1 μm and thickness of 2–7 nm, as shown in Fig. S1. These composite powders were created using a planetary ball mill machine (Changsha Tianchuang Powder) with a disk rotation speed of 300 rpm and a milling time of 10 h. The microstructure of the mixed 316 L powder is illustrated in Fig. 1, along with their energy dispersive spectrometer (EDS) mapping. The analysis indicates that there was no significant alteration in the sphericity and particle size of the mixed powder, while the graphene powder was uniformly adhered to the surface of the 316 L powder.

The LPBF machine utilized in this study was the EOS device (M100, Germany). A scanning strategy involving a 60° rotation between layers was employed, as illustrated in Fig. 2a. The established processing parameters included a laser power of 100 W, scanning speed of 1000 mm/s, layer thickness of 20 μm, and hatch spacing of 80 μm. Fig. 2b displays the fabricated samples, which comprised a dog-bone-shaped tensile sample, a cylindrical compression sample, and a square corrosion/friction sample. Each sample was labeled based on the graphene content added: 0.1 wt% graphene, 0.2 wt% graphene, 0.3 wt% graphene, with the sample without graphene denoted as LPBF-316 L.

2.2. Microstructural characterization

Before micro-characterization, different samples were mechanically ground with emery paper ranging from 80 to 200 grit size, and polished with alumina suspension followed by a suspension of colloidal Silica successively. Ultimately, use an ethanol solution with a purity of 99.99% for rinsing. The phase composition is identified utilizing an X-ray diffraction (XRD, SHIMADZU XRD-7000, Japan) with Cu Kα radiation at 40 kV and 30 mA, and the scanning speed was 2°/min and the scanning range was 30°–90°. The microstructure was observed by scanning electron microscope (SEM, ZEISS EV018, Germany) respectively, and the energy dispersive spectroscopy (EDS, Oxford, UK) of the SEM was used to analyze the composition of the samples. In addition, electropolishing was done before electron backscattered diffraction (EBSD, Oxford, UK), with a solution consisting of perchloric acid and methanol mixed in a ratio of 20:80 at 12 V for14 s maintaining at 15 °C. It is mainly used to express the grain size, texture strength and direction of the sample.

2.3. Electrochemical, mechanical properties and friction experiments

For electrochemical experiments, the corrosion resistance of the

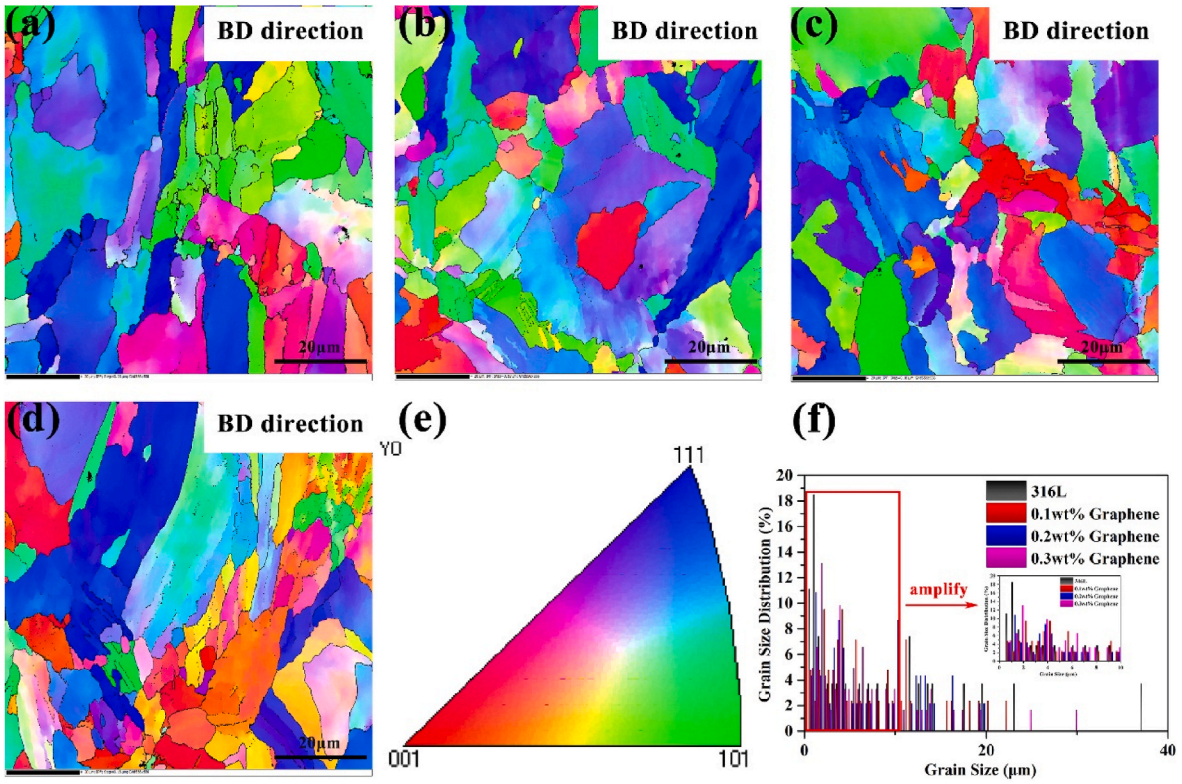

Fig. 7. EBSD map of LPBF-316 L with and without graphene addition: (a) LPBF-316 L (b) 0.1 wt% graphene, (c) 0.2 wt% graphene (d) 0.3 wt% graphene (e) Euler angles with different color, (f) Grain size distribution of LPBF-316 L samples with different graphene contents. (For interpretation of the references to color in this figure legend, the reader is referred to the Web version of this article.)

samples was evaluated by an electrochemical workstation (three-electrode system) in 3.5 wt% NaCl. The sample (1 cm^2) was connected to the working electrode, and the saturated calomel electrode and platinum sheet were connected to the reference electrode and the reverse electrode, respectively. First, the sample was soaked in the solution for 1 h to ensure a stable open circuit potential. Electrochemical impedance spectroscopy (EIS) is measured in the frequency range of 10^{-2} Hz–10^5 Hz (interference potential 10 mV). The polarization curve is measured in the voltage range from −0.5 V to 0.5 V (scan rate 1 mV/s). In addition, the experiment needs to choose an appropriate scanning rate. When the scanning rate is too fast, the electrode potential changes too fast, and the measured polarization curve may deviate from the actual value, while the scanning rate is too slow, and the test period will be prolonged. Finally, we chose a more suitable scan rate of 1 mV/s. Corrosion current density (I_{corr}) and corrosion potential (E_{corr}) were obtained by the Tafel extrapolation method. To evaluate the long-term corrosion resistance and stability of the material, the immersion test was carried out in 3.5 wt % NaCl for 360 h. During the experiment, EIS measurement was carried out at a specific time node to detect the change in corrosion resistance. After soaking, the surface morphology and composition of the material were analyzed by SEM and EDS. The test of mechanical properties is tensile tests carried out on the KQL computer-controlled electronic universal testing machine with the loaded strain rate is 3×10^{-4} s^{-1}, universal tensile testing machine with a capacity of 10 kN at room temperature. Three successive tests were conducted for each sample. The fracture morphology was characterized by SEM. The broken surface is carefully cleaned and any contaminants are removed with ethanol ultrasound. And the surface nature of failure in tensile coupons of each sample were analyzed. In addition, Viker's hardness of the specimens were recorded by a micro-hardness testing machine at an applied load of 500 g. And 5 data points were collected for averaging the hardness of the specimens. Furthermore, the nanoindenter (Anton Paar Step-NHT3, Austria) was used to measure the nano-hardness, and the indentation adopted a load of 20 mN, and pause 5 s. The friction experiments are carried out by multifunctional friction and wear testing machine (MFT-5000, Rtec, US). The friction counterpart was a 4 mm stainless steel quenched steel ball with a reciprocating stroke of 5 mm, an applied load of 30 N, a friction speed of 5 Hz, and a time of 30 min.

3. Results and discussion

3.1. Microstructure

Fig. 3 illustrates the X-ray diffraction (XRD) results of both powder and processed bulk samples. The analysis shows that both the powder and bulk samples exhibit a single austenitic γ phase, with no martensitic phase detected in the 316 L sample produced via LPBF. A comparison between the XRD spectra of 316 L powder and bulk samples reveals that the diffraction peak of the pure 316 L block becomes broader post LPBF treatment, indicating the presence of residual stress leading to peak broadening. The introduction of graphene mitigates this effect, resulting in a negligible increase in peak width, suggesting that graphene incorporation aids in reducing residual stress levels [24]. In addition, the distortion of crystal faces due to residual stress from rapid melting and solidification during laser processing can contribute to peak broadening [25–27]. Moreover, diffraction peak broadening is influenced by lattice defects, microscopic distortions resulting from irregular atomic positions in the lattice, and variations in grain size introduced during the printing process. Notably, the addition of graphene causes a leftward shift in the diffraction peak of the bulk sample, possibly attributed to an expansion in lattice constant within the matrix at sub-grain boundaries induced by graphene doping [28].

In Fig. 4, perpendicular to the printing direction, the laser additive manufacturing process involves a layer-on-layer superposition process, resulting in a well-organized and regular melt pool due to repeated scanning. However, the previously solidified matrix is partially remelted

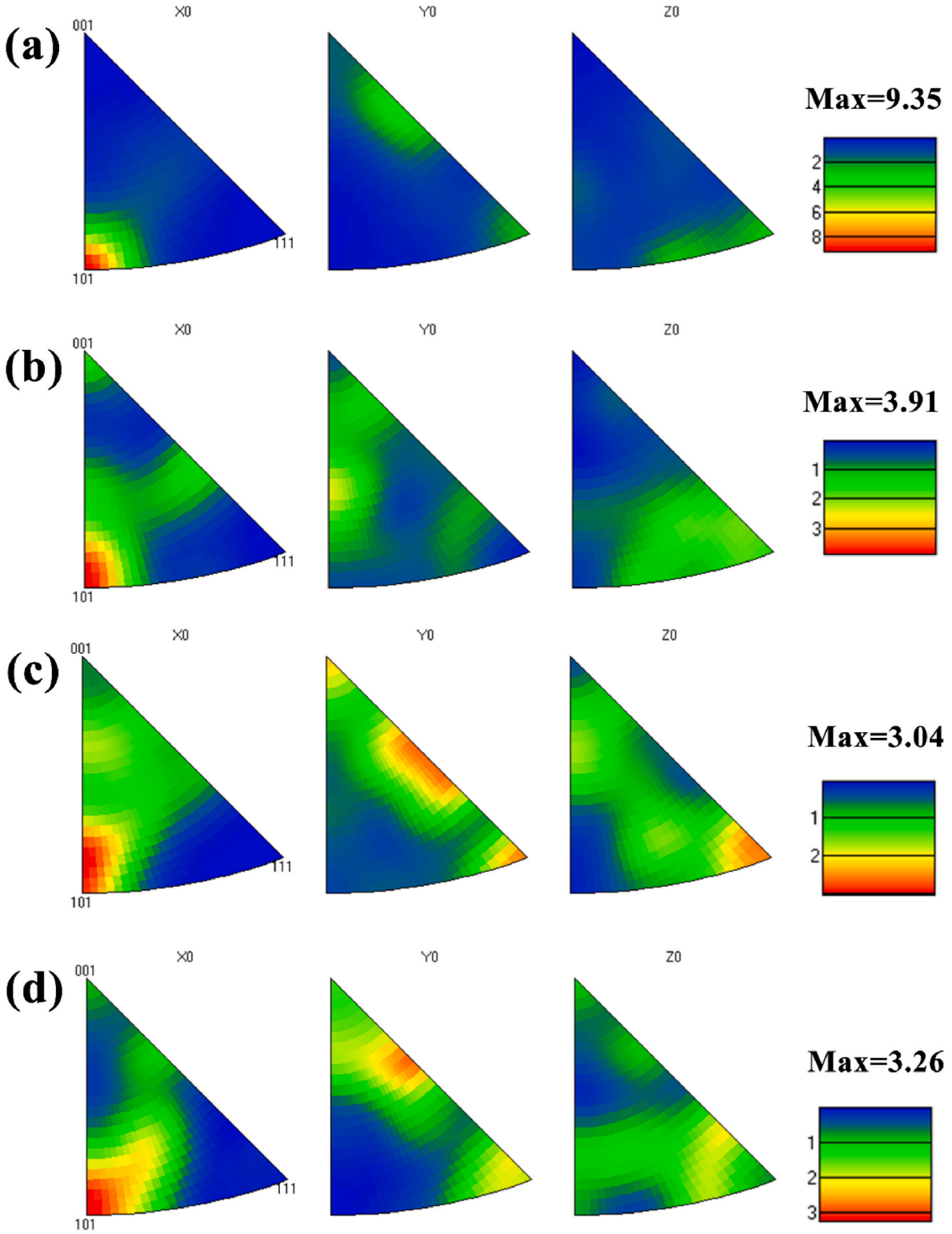

Fig. 8. Pole figures (PF) along with LPBF-316 L with different graphene, (a) LPBF-316 L (b) 0.1 wt% graphene, (c) 0.2 wt% graphene (d) 0.3 wt% graphene.

during the next laser scanning, leading to the formation of large-size columnar crystals. Notably, the addition of graphene transforms some columnar crystals into equiaxed crystals, achieving grain refinement. Furthermore, the incorporation of 0.2 wt% graphene results in the formation of more equiaxed crystals, enhancing the grain refinement effect.

Fig. 5 depicts the microstructure and morphologies of LPBF-316L/graphene composites from a top view. A black, flaky precipitate is observed in the sample with added graphene, with its amount gradually increasing as the graphene content increases. To further analyze this precipitate's composition, a line scanning was conducted on the precipitated area, as illustrated in Fig. 6. The carbon content significantly increased in the black material region, while the levels of elements such as Fe, Cr, and Ni remained relatively unchanged. This indicates that the graphene addition did not lead to carbide formation, and the graphene still exists in the form of nanoplatelets without undergoing interfacial chemical reactions with the stainless steel matrix

Table 1
Parameters obtained from polarization curves of different samples.

Samples	E_{corr} (V vs.SCE)	I_{corr} (A/cm^2)
316 L	−0.25 ± 0.3	8.05 ± 0.6 × 10^{-7}
0.1 wt % graphene	−0.26 ± 0.2	1.45 ± 0.7 × 10^{-7}
0.2 wt% graphene	−0.24 ± 0.2	6.61 ± 0.8 × 10^{-8}
0.3 wt% graphene	−0.28 ± 0.3	3.12 ± 0.6 × 10^{-7}

[29].

Different sample inverse pole figures (IPF) were displayed in Fig. 7a-(d), showcasing various colors corresponding to grain orientation relative to the lattice, with each color representing a unique combination of Euler angles as shown in Fig. 7e. Consequently, grains sharing the same crystal orientation exhibit similar colors. Additionally, the average grain sizes of the different samples were determined and illustrated in Fig. 7f. The IPF of pure 316 L exhibited the common epitaxial columnar grain structure observed in other LPBF-processed alloys [30]. Upon the introduction of graphene, the columnar crystal growth transitioned to equiaxed crystals, resulting in a noticeable grain refinement effect, with calculated average grain sizes of 8.18 μm (LPBF-316 L), 7.16 μm (0.1 wt % graphene), 5.57 μm (0.2 wt% graphene), and 7.29 μm (0.3 wt% graphene). This grain refinement phenomenon is attributed to the abundant heterogeneous nucleation sites provided by graphene, enhancing nucleation rates and promoting grain refinement [31–33]. Furthermore, the graphene particles enhance laser absorption of the composite powder, effectively increase the temperature gradient of the molten pool, elevate supercooling levels, and further boost nucleation rates [23]. Moreover, graphene nano-scale particles or plates within a metal matrix can impede grain growth. However, the addition of 0.3 wt % graphene may lead to grain coarsening, primarily due to excessive precipitate concentration weakening hindrance to grain boundary migration and accelerating grain growth. The aggregation, non-uniform dispersion, and inhomogeneity resulting from excessive graphene addition also contribute to increased grain size [34,35]. Intriguingly, the presence of graphene does not appear to affect the prominent orientation based on color distribution.

As depicted in Fig. 8, the texture of the grains exhibits strength in the [101] direction, with varying intensity levels. The texture index decreases from 9.35 in LPBF-316 L to 3.91, 3.04, and 3.26 in samples with different graphene contents. This is mainly due to the addition of nucleating particles, which weakened the epitaxial growth trend of LPBF-316 L and reduced the anisotropy of the texture [20]. A high

Table 2
The fitted values of EIS measurements.

Samples	R_s (Ω·cm^2)	CPE S s^n cm^2		R_{ct} (Ω·cm^2)
		Y_0(Ω^{-1}cm^{-2}s^n)	n	
316L	41.2 ± 3.4	1.3 ± 0.2 × 10^{-5}	0.97 ± 0.4	3.7 ± 0.2 × 10^5
0.1 wt% graphene	49.7 ± 4.7	8.6 ± 0.3 × 10^{-6}	0.90 ± 0.2	5.8 ± 0.3 × 10^5
0.2 wt% graphene	50.3 ± 3.3	7.3 ± 0.2 × 10^{-6}	0.87 ± 0.3	7.3 ± 0.2 × 10^5
0.3 wt% graphene	46.8 ± 4.2	1.1 ± 0.3 × 10^{-5}	0.91 ± 0.2	5.2 ± 0.3 × 105

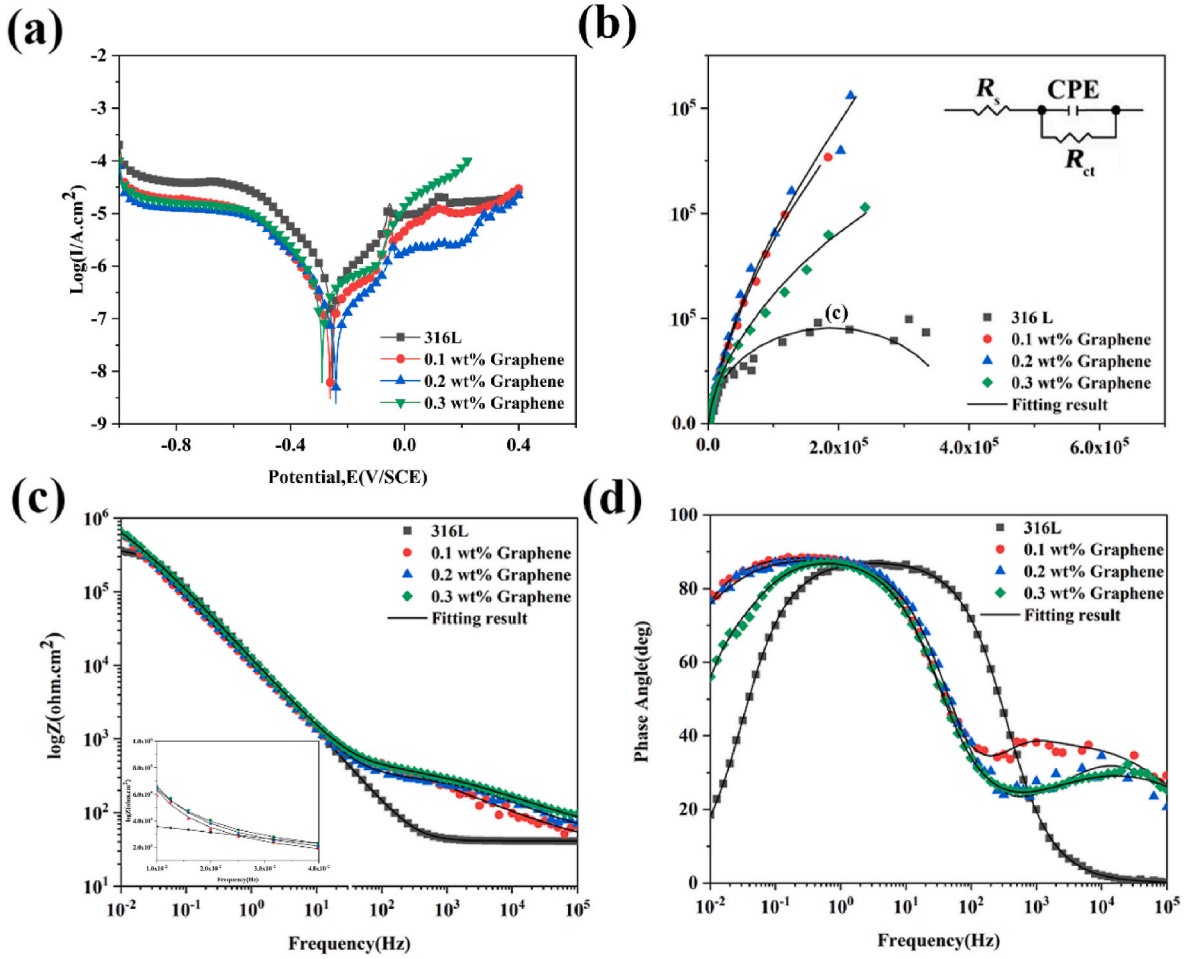

Fig. 9. Electrochemical tests (a) Polarization curves, (b) Nyquist plots, (c) Bode plots of |Z| vs. frequency, (d) Bode plots of phase angle vs. frequency.

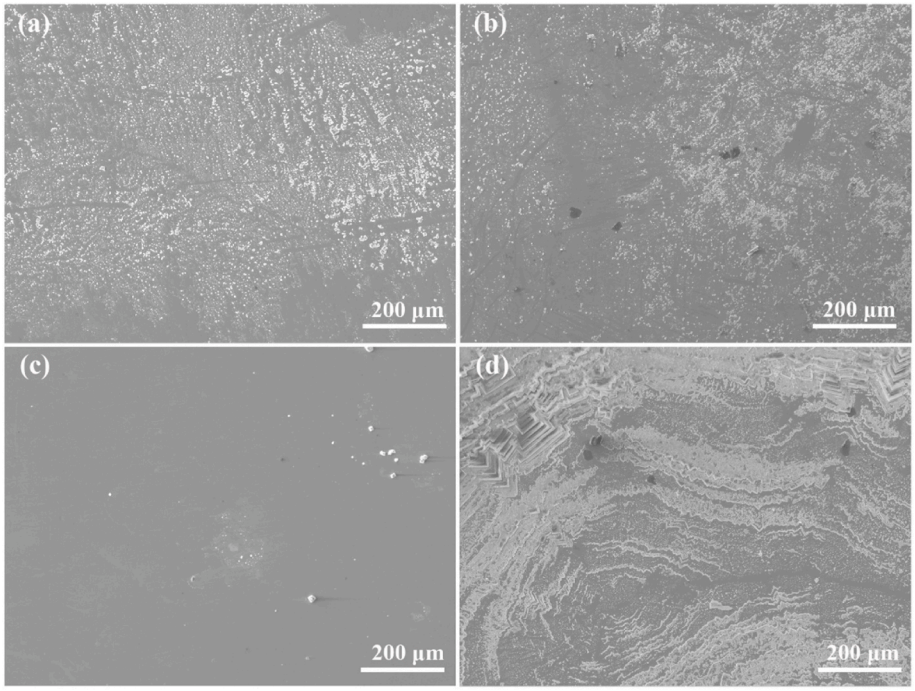

Fig. 10. SEM of samples after electrochemical testing: (a) LPBF-316 L, (b) 0.1 wt % graphene (c) 0.2 wt % graphene, (d) 0.3 wt % graphene.

texture index suggests a pronounced texture inclination and a distinct anisotropic structure in LPBF-316 L. Upon the incorporation of graphene, the maximum texture index in 316L-0.2 wt% graphene reduced to 3.04, leading to a notable weakening of the anisotropic trend and a gradual shift towards an isotropic microstructure. This phenomenon is likely due to the presence of nucleating particles in additively manufactured alloys, which are anticipated to diminish the texture [20]. Furthermore, we conducted analyses on phase distribution maps, Kernel Average Misorientation maps (KAM), and Schmid Factor maps (SF) (refer to Figs. S2–S4). Despite this, it appears that the addition of graphene had minimal impact on the phase composition and KAM. Generally, according to the geometric dislocation density formula $\rho GND = 2KAM_{ave}/\mu b$, which KAM_{ave} is the average value of KAM, μ is the step size chosen for the EBSD experiment and b is the length of the Burgers vector. The density of geometrically necessary dislocations is closely related to KAM and shows a positive linear relation with the average of KAM [36–38]. The findings indicate that the FCC phase in the matrix remained unaffected by the inclusion of graphene (the results are consistent with XRD), and the geometrically necessary dislocations within the matrix did not alter due to graphene addition [39]. Notably, in the SF images, different colors represent varying SF values, with SF primarily distributed between 0.3 and 0.5. The proportion of LPBF-316 L samples with SF values exceeding 0.35 is slightly lower than that of LPBF-316 L-graphene samples, particularly evident in the 0.2 wt% graphene sample (96.7%).

3.2. Electrochemical corrosion behavior

To investigate the impact of graphene on the corrosion resistance of LPBF-316 L, both short-term electrochemical experiments and long-term immersion experiments were conducted. The corresponding I_{corr} and E_{corr} values (Table 1) were derived from the results of the polarization curve (Fig. 9a). All three graphene-doped samples exhibited lower corrosion current densities compared to the 316 L samples ($8.05 \pm 0.6 \times 10^{-7}$ A/cm^2). Among these, the sample with 0.2 wt% graphene demonstrated the lowest corrosion current density ($6.61 \pm 0.8 \times 10^{-8}$ A/cm^2). A decrease in corrosion current typically indicates higher corrosion resistance and improved chemical stability [40–42]. The enhanced corrosion resistance observed after adding graphene may stem from its ability to impede ion transfer between the electrolytic solution and slow down the reaction of the corrosion solution with the metal surface [43]. The obvious passivation was observed in the polarization curve of 0.2 wt % graphene samples, indicating that the oxide film formed on the metal surface can protect the matrix. In addition, the study shows that the increase of grain refinement can also improve the corrosion resistance of the material. After doping graphene, the grain size of the material is refined, which reduces the corrosion hazard to a certain extent [44,45].

Fig. 9 (b)–(c) shows the EIS results for four samples. In the Nyquist diagram, the diameter of the capacitor ring can reflect the corrosion resistance of the sample, and the larger the diameter size means the better the corrosion resistance [46]. The Nyquist diagram shows that the three samples doped with graphene show large capacitive ring diameters, and the 0.2 wt% graphene sample has the largest diameter. At the same time, graphene-doped samples also have higher |Z| values at low-frequency, and higher Bode phase angles at medium-frequency. All these indicate that the corrosion resistance of doped graphene samples is better, which is consistent with the polarization curve results [47]. To explain the corrosion behavior in depth, an equivalent circuit (EC) with a time constant is introduced. Among them, R_s represents the solution resistance of the corrosive fluid, R_{ct} represents the charge transfer resistance, and CPE represents the constant phase element. R_{ct} correlates with corrosion behavior, and 0.2 wt% graphene samples exhibit the highest R_{ct} value ($7.3 \pm 0.2 \times 10^5$ Ω cm^2), indicating the best corrosion resistance. CPE can be calculated from $Y_{CPE}(j\omega) = [Y_0 (j\omega)^n]^{-1}$, where Y_0 is the admittance and n is the power index. The Y_0 value of the 316 L sample is higher than that of the graphene-doped sample, indicating that the surface corrosion area is larger and the corrosion resistance is poor [48]. All the above results indicate that doped graphene powder can improve the corrosion resistance of 316 L samples (see Table 2).

The corrosion morphology (Fig. 10) was observed by electron microscope after the corrosion experiment. A large number of corrosion products appeared on the surface of 316 L samples after soaking, the corrosion reaction was severe, and the corrosion products decreased after doping graphene. Among them, the surface of the doped 0.2 wt % graphene sample (Fig. 10c) is still smooth after corrosion, and the

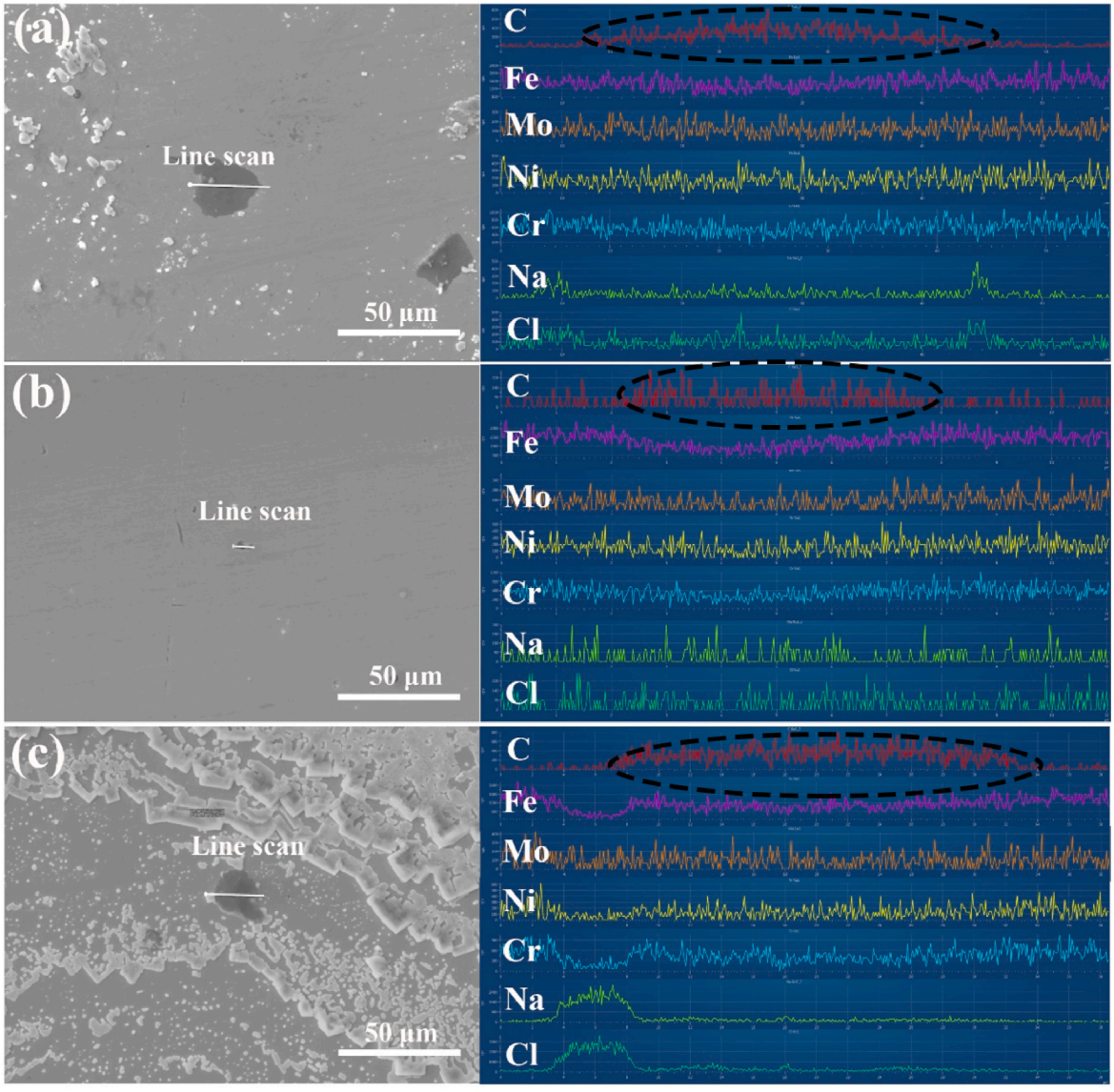

Fig. 11. EDS line scanning of the samples after electrochemical testing: (a) 0.1 wt % graphene, (b) 0.2 wt % graphene, (c) 0.3 wt % graphene.

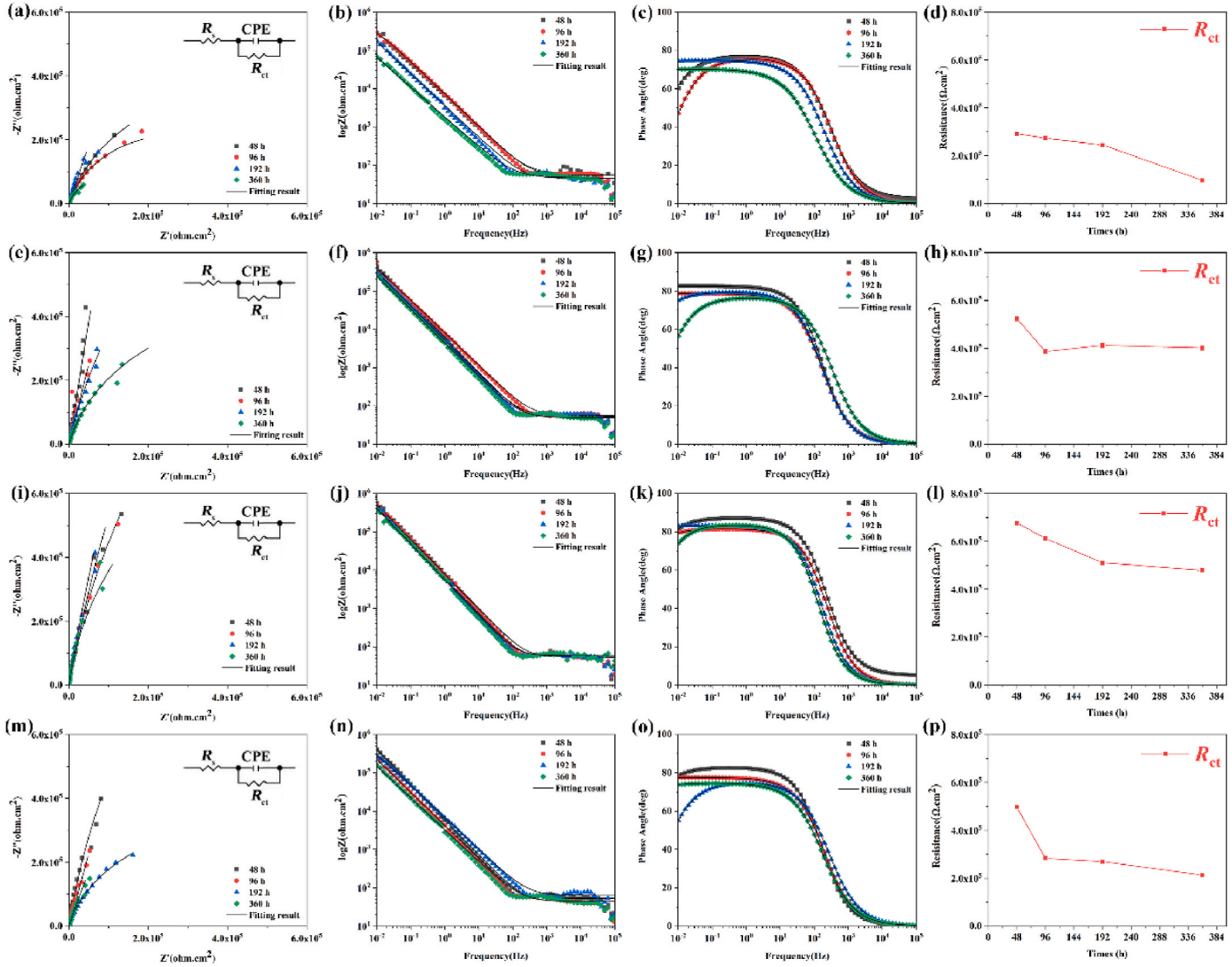

Fig. 12. EIS curves and the fitted results of samples immersed in NaCl for 360 h (a–d) 316 L, (e–h) 0.1 wt % graphene sample, (i–l) 0.2 wt % graphene sample, (m–p) 0.3 wt % graphene sample.

corrosion products are few, indicating that the 0.2 wt % graphene sample has the best corrosion resistance. This is consistent with the potentiodynamic test results. In addition, EDS line scanning was used to detect the components of the precipitates after corrosion of doped graphene samples (Fig. 11). The main element of the precipitate is C element aggregation, which means that the precipitate is mainly graphene. There are fewer corrosion products around the precipitates, indicating that graphene can slow down the corrosion reaction.

The long-term immersion test assesses the corrosion resistance and stability of the sample over time. In Fig. 12, the EIS test results and corresponding R_{ct} values during the soaking process are depicted. As the soaking time increased, the diameters of the four sample types decreased to varying degrees. Notably, the doped graphene sample consistently exhibited a larger capacitive ring size compared to the 316 L sample throughout the immersion process. The Bode plot and R_{ct} value also confirmed this observation. This may be due to the fact that the presence of graphene powder effectively reduce the grain size of 316 L, thus hindering the corrosion of the solution on the matrix and improving the long-term corrosion resistance [44].

After soaking, the surface morphology and element composition of the sample were analyzed. The graphene-doped sample exhibited a decrease in Cl^- attached to the surface, indicating enhanced long-term stability compared to the original sample (Fig. 13). Furthermore, the study revealed that the 0.2 wt% graphene sample did not show the Cl^- on the surface, in contrast to the 0.1 wt% and 0.3 wt% graphene samples. EDS line scanning analysis of the uncorroded black area identified C element aggregation as graphene (Fig. 14). The absence of Cl^- around graphene suggests its ability to resist Cl^- erosion due to its excellent chemical stability and impermeability [49]. Therefore, the inclusion of graphene not only maintains corrosion resistance but also enhances it.

3.3. Mechanical behavior

Fig. 15 shows the stress-strain curves of LPBF-316 L with and without graphene at room temperature. In tensile curves, graphene-added samples showed significant increases in yield fracture strength and ductility, reaching the highest value when the graphene content reached 0.2 wt%, as shown in Table 3. The increase in strength can be attributed to a variety of strengthening mechanisms: grain refinement [19,50], Orowan strengthening [16,51] and thermal mismatch precipitation strengthening [52], etc. Fig. 16 illustrates the SEM micrograph of the tensile fracture surfaces of the samples at different magnifications. For pure LPBF-316 L samples, there are some shallow and uniform dimples at the fracture, which is a typical image of ductile fracture. Meanwhile, some river-like fracture morphology can be observed at the local fracture surfaces, which is the typical morphology of brittle-like behavior. This

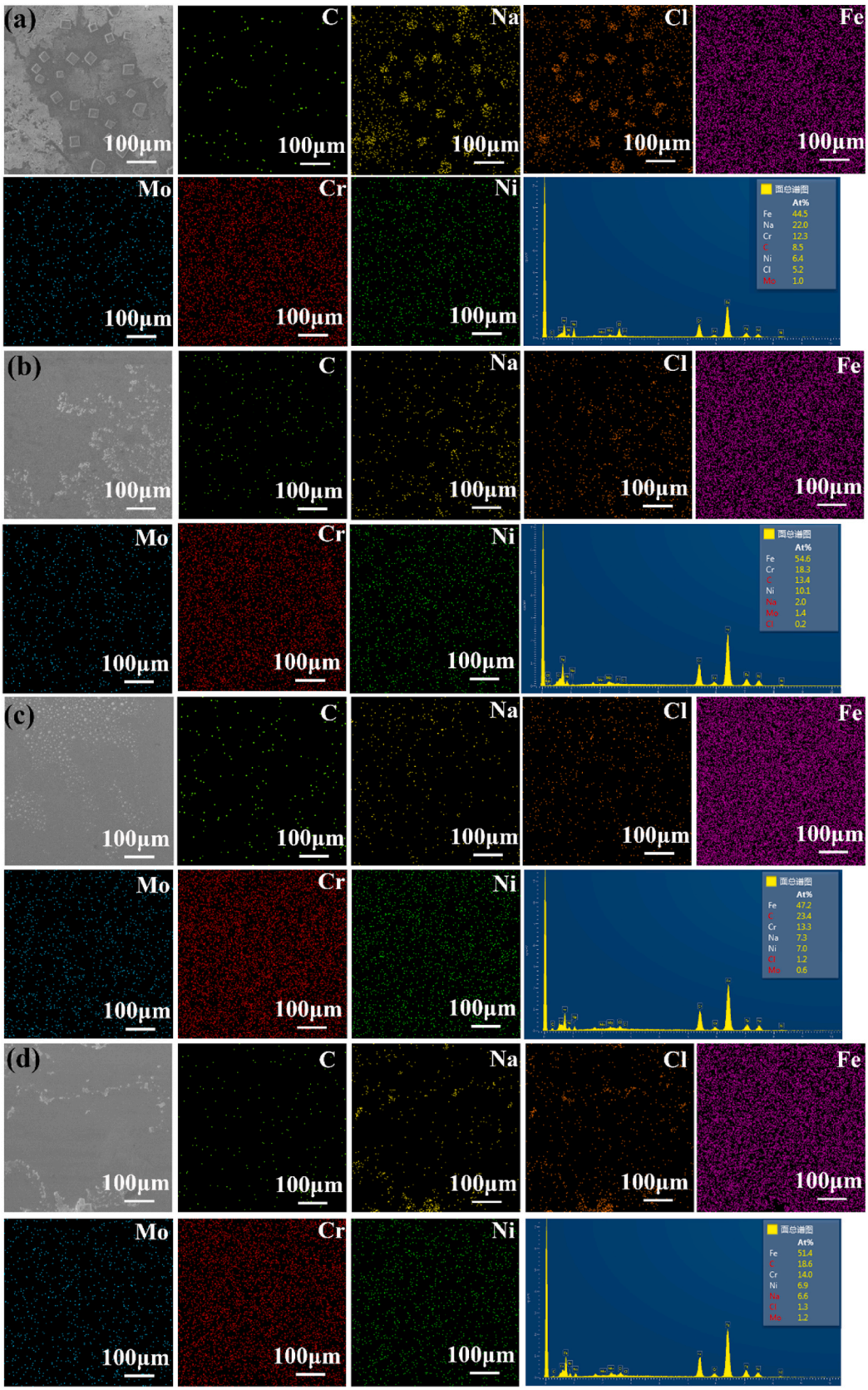

Fig. 13. SEM images and EDS analysis of the samples after immersion for 360 h: (a) LPBF-316 L, (b) 0.1 wt % graphene, (c) 0.2 wt % graphene, (d) 0.3 wt % graphene.

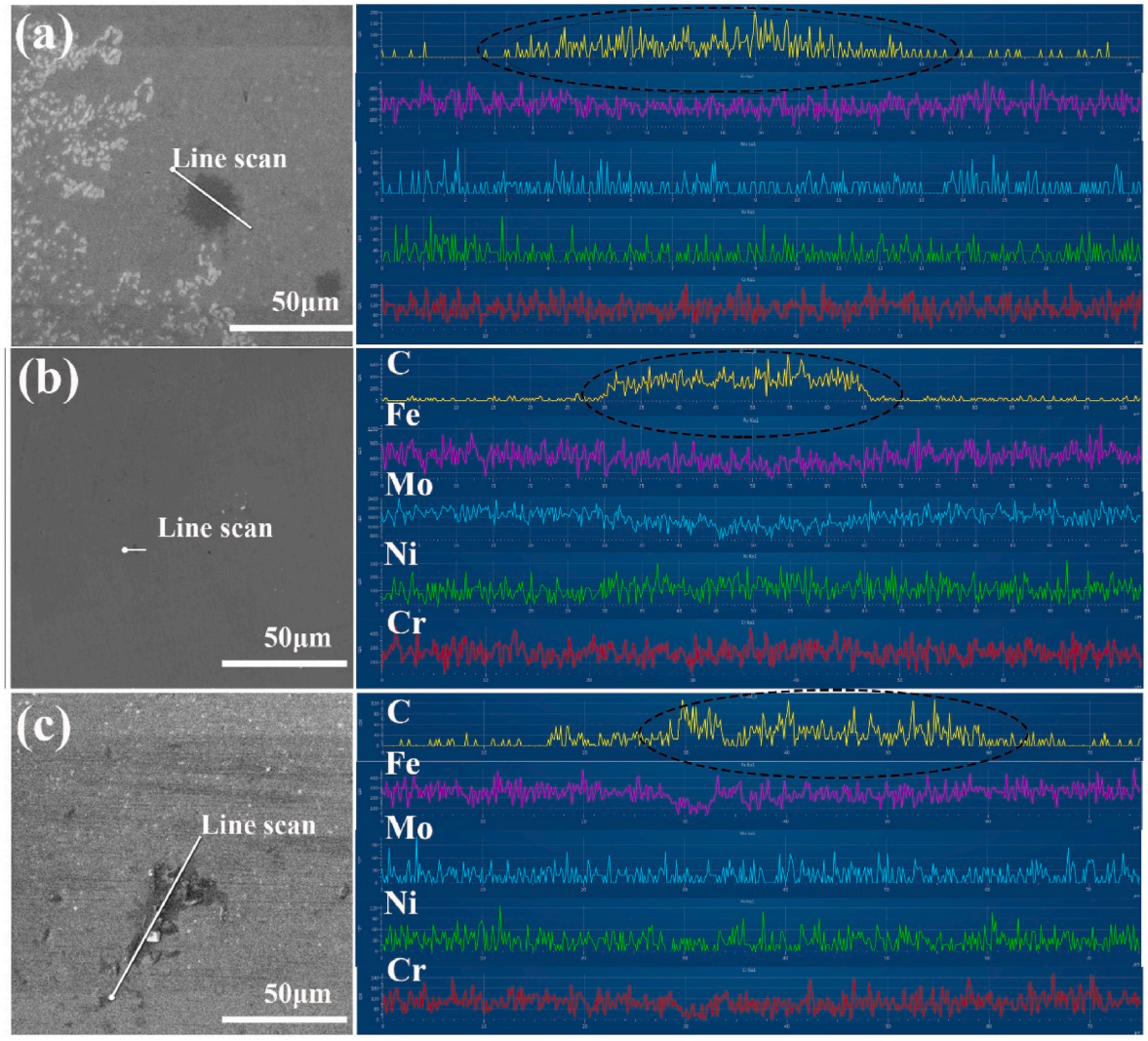

Fig. 14. EDS line scanning of the samples after immersion for 360 h: (a) 0.1 wt % graphene, (b) 0.2 wt % graphene, (c) 0.3 wt % graphene.

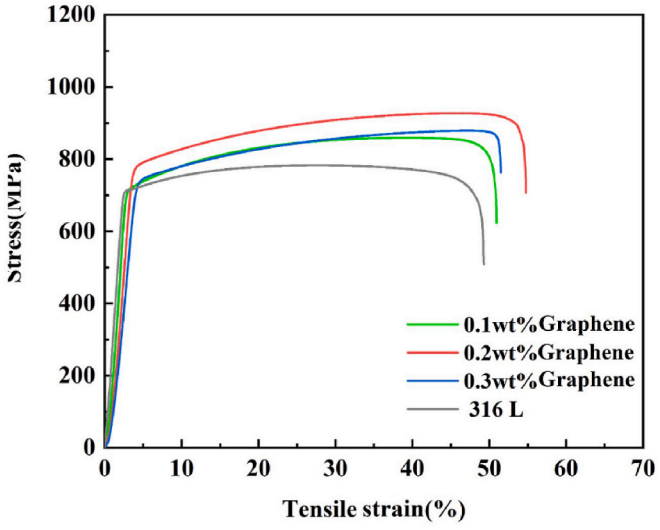

Fig. 15. Stress-strain curves of LPBF-316 L and LPBF-316 L with graphene.

Table 3
The tensile and compress properties of LPBF-316 L with and without graphene.

Experiment	Result	LPBF −316 L	0.1 wt% graphene	0.2 wt% graphene	0.3 wt% graphene
Tensile	Yield strength (MPa)	714.04	714.8	780.2	737.5
	Ultimate strength (MPa)	764.9	859.3	927.4	878.5
	Elongation (%)	49.27	50.93	54.75	51.5

phenomenon indicates that the specimen with a mixed fracture mode of the cleavage fracture and the dimple fracture. The addition of graphene resulted in the apparent disappearance of river-like areas, and a significant increase in dimple and an increase in density, especially the addition of 0.2 wt% graphene, which may be the main reason for the improved ductility. In addition, nanosphere-type oxide particles were found in the samples added to graphene, and due to the very small size of the oxides, they have little influence on uniform plastic deformation, due to the cracks not forming easily and the fracture occurring only when the small voids extended and linked up. At the same time, the

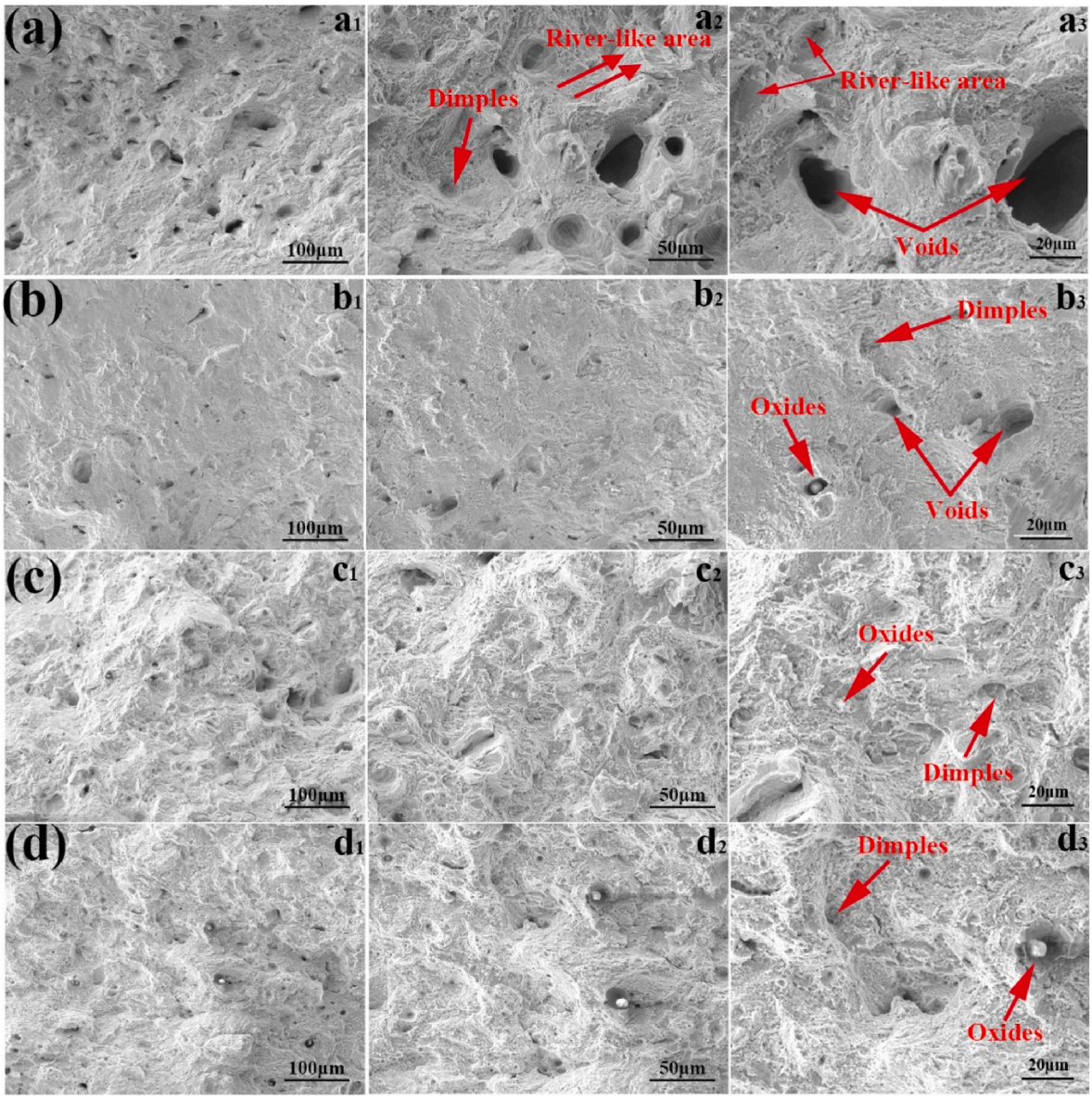

Fig. 16. SEM images showing cross-sections of the fracture surface, (a) LPBF-316 L, (b) 0.1 wt% graphene, (c) 0.2 wt% graphene, (d) 0.3 wt% graphene.

addition of graphene to reduce defects such as voids at the fracture is also one of the reasons for increased ductility [53].

3.4. Friction behavior

Fig. 17a shows the friction coefficient curves (COF) of different samples. The COF decreased with the addition of graphene, which due to the solid lubrication properties of graphene to form a self-lubricating film [54,55]. It's very soft and can prevent direct metal-to-metal contact during sliding. In addition, the Vicker hardness and nano-hardness values of the LPBF-316 L with different graphene contents are shown in Fig. 17b–d. The Vickers hardness value for LPBF-316 L and the composites with 0.1 wt%, 0.2 wt% and 0.3 wt% graphene were 252 V, 273 HV, 329 HV and 296 HV respectively. The nano-hardness values were 192 GPa, 230 GPa, 251 GPa and 232 GPa. This result shows that the addition of graphene leads to an increase in both Vickers hardness and nano-hardness. The grain refinement brought about by the addition of graphene, the reduction of residual stress and the change of lattice constant shown in XRD results may be the main reasons for the increase in hardness [52,56,57]. Of these, the 0.2 wt% graphene sample has the lowest COF due to its highest hardness and smallest grain size, which approaches about 0.4 at stability, lower than LBF-316 L (~0.6). This also shows that hardness and grain size play a major role in reducing COF.

The surface morphology, three-dimensional morphology and scratch depth of different samples after wear are shown in Fig. 18. From the SEM images, it can be clearly observed that there are mild patches on the wear tracks, indicating that the worn form is mainly micro-ploughing. At the same time, the grooves in the LPBF-316 L sample were significantly deeper than those in the composite sample (Fig. 18a_4-d_4). It has been proved that the addition of graphene makes the wear surface smoother, the wear track becomes shallower and finer and effectively strengthens the anti-wear ability. Additionally, the low hardness of the LPBF-316 L is also the main reason for the formation of deep grooves during sliding.

To further analyze the wear mechanism, the wear surfaces of different samples were amplified. It can be clearly found that in all the samples in addition to the obvious micro-ploughing, there are still micro-abrasive wear and adhesive wear (Fig. 19). Among them, the addition of 0.2 wt% graphene, due to increased hardness and enhanced surface lubrication, shows a smaller adhesive wear area and a shallower wear depth. And further proved that the wear resistance of the

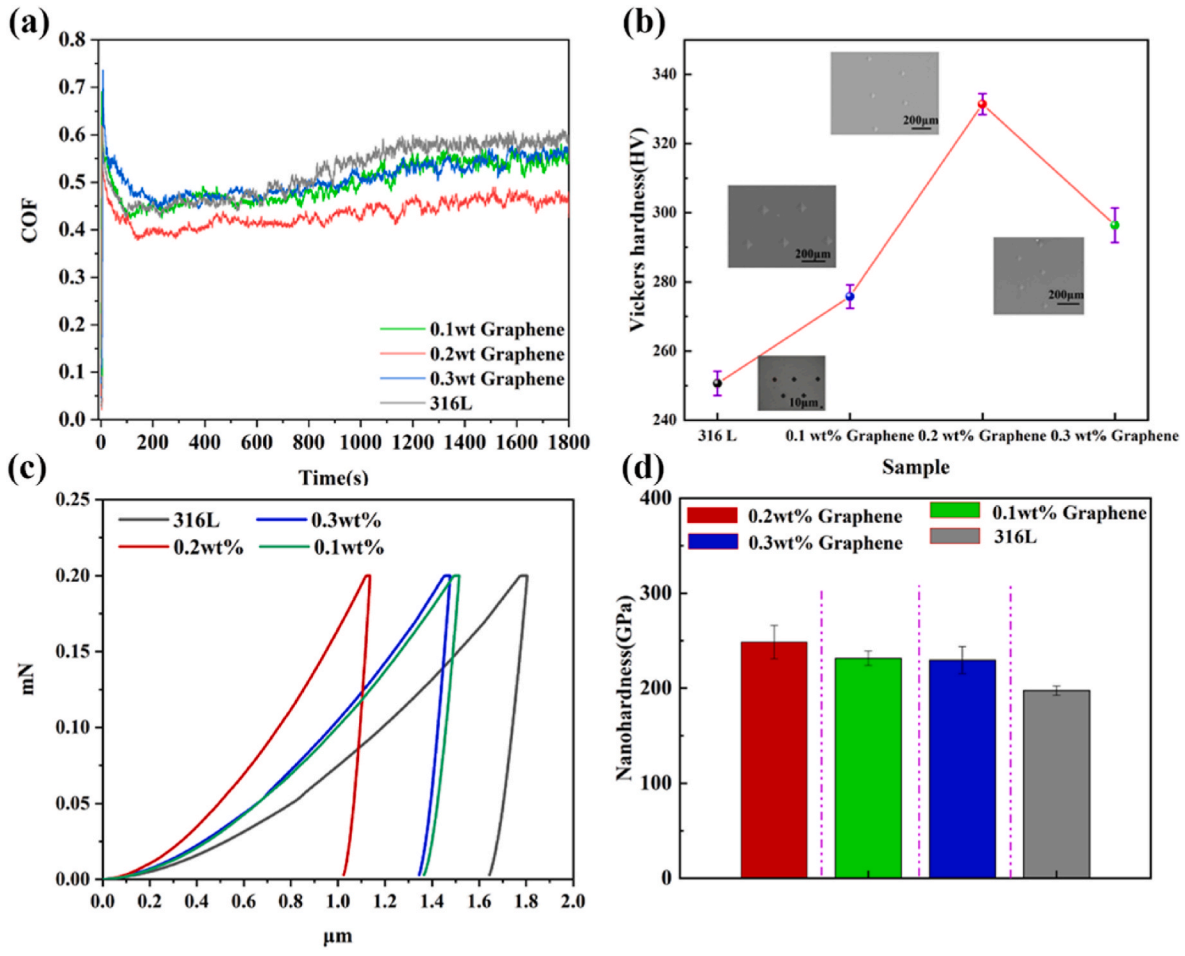

Fig. 17. (a) Friction coefficient curve, (b) Vickers hardness of different samples, (c) Load-displacement curve, (d) Nano-hardness of different samples.

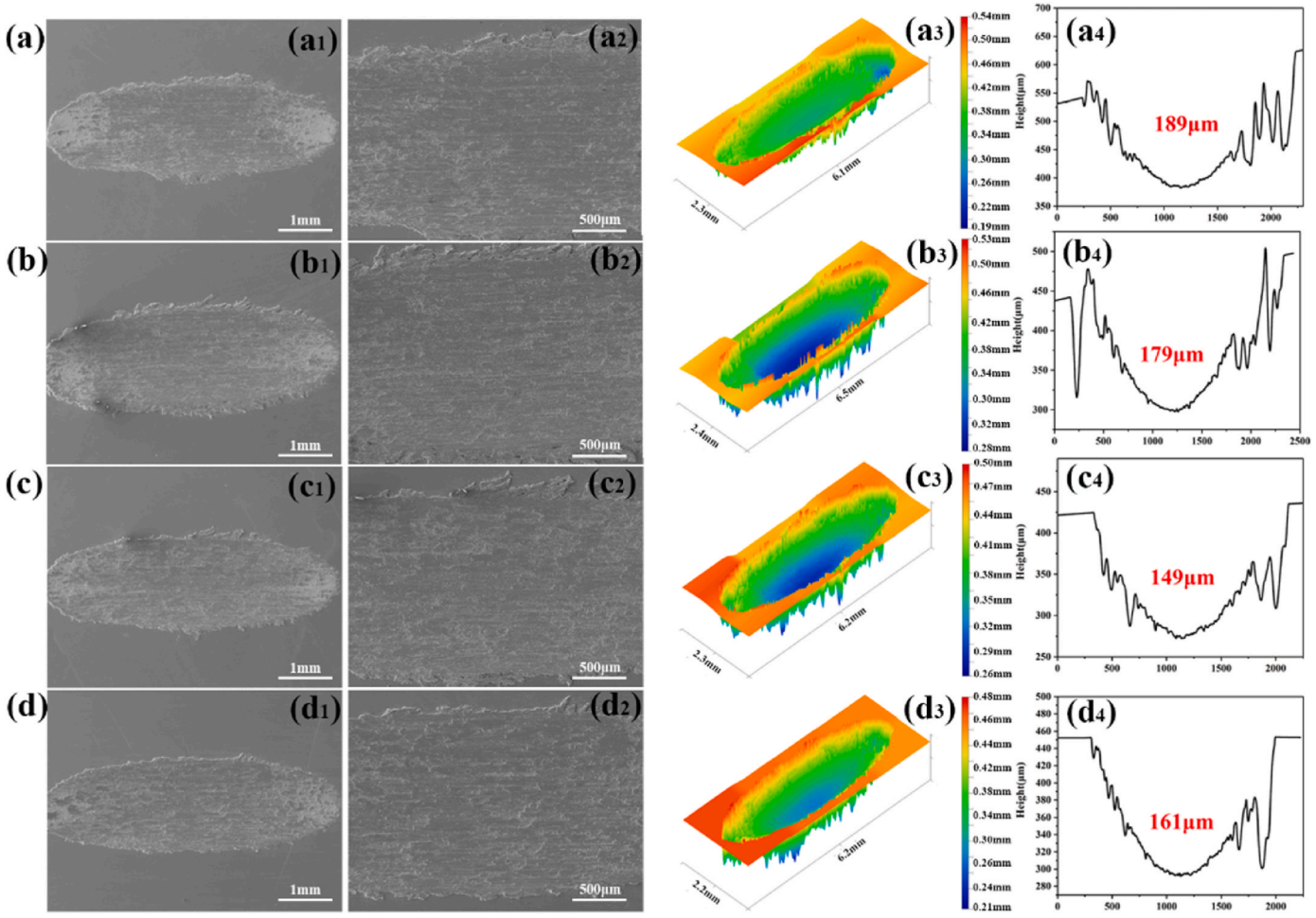

Fig. 18. 2D and 3D morphologies of abrasion of different samples, (a) LPBF-316 L, (b) 0.1 wt% graphene, (c) 0.2 wt% graphene, (d) 0.3 wt% graphene.

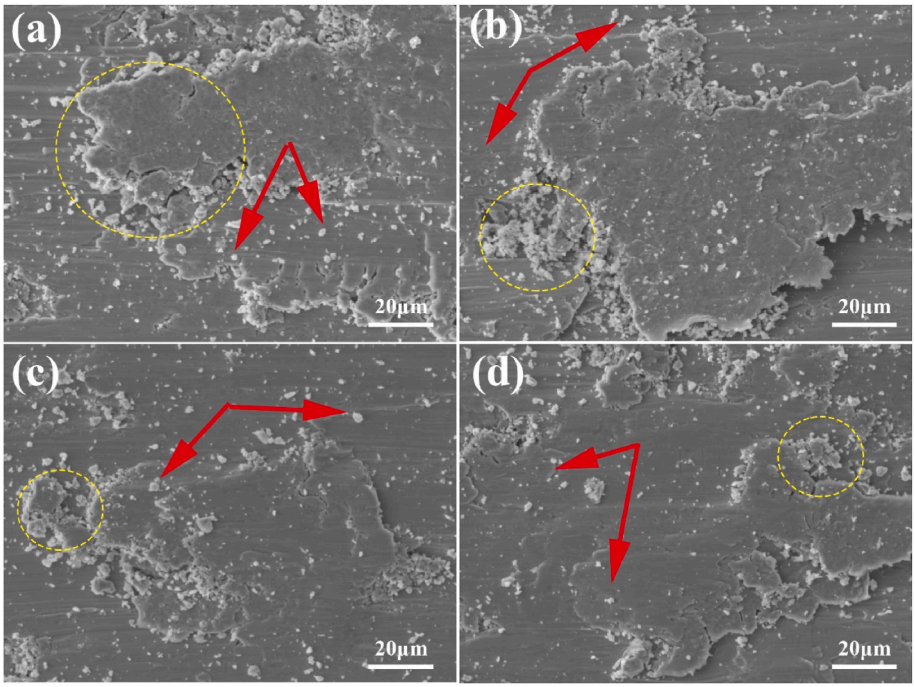

Fig. 19. 2D morphologies of abrasion after magnification of different samples, (a) LPBF-316 L, (b) 0.1 wt% graphene, (c) 0.2 wt% graphene, (d) 0.3 wt% graphene.

composite is improved.

4. Conclusion

The graphene-modified LPBF-316 L composite was successfully prepared, and its corrosion resistance, mechanical properties and tribological performance were comprehensively investigated. The addition of graphene improved the mechanical and friction resistance while ensuring or even improving the corrosion resistance. The key findings of the present study are as follows:

(1) The addition of graphene does not form intermetallic compounds with the 316 L, while dispersed in the matrix in the form of C element uniformly, and increases with the increase of the amount of graphene added.
(2) The addition of graphene resulted in the refinement of the grains and weakened the strong texture in the direction of <101>. The grain size of 0.2 wt% graphene is reduced to 5.57 μm and the texture strength is reduced to 3.04.
(3) Both in terms of short-term and long-term corrosion resistance, the graphene-modified LPBF-316 L composite demonstrated up to an order of magnitude reduction in I_{corr} compared to the original sample.
(4) The addition of graphene successfully achieved a synergistic improvement of mechanical strength and ductility, and the tensile fracture strength and ductility of 0.2 wt% graphene sample was increased by 20% and 5.48%, respectively.
(5) Compared with LPBF-316 L, graphene-enhanced 316 L has good self-lubricating properties, higher wear resistance and lower COF. And the worn form is mainly micro-ploughing, the wear mechanism is micro-abrasive wear and adhesive wear.

Declaration of competing interest

The authors declare that they have no known competing financial interests or personal relationships that could have appeared to influence the work reported in this paper.

Acknowledgments

This work is supported by the National Key Research and Development Program of China (Grant 2022YFB4600500) and the National Natural Science Foundation of China (Grant 52235006 and 52025053).

Appendix A. Supplementary data

Supplementary data to this article can be found online at https://doi.org/10.1016/j.jmrt.2024.06.061.

References

[1] Wang YM, Voisin T, McKeown JT, et al. Additively manufactured hierarchical stainless steels with high strength and ductility. Nat Mater 2018;17(1):63.
[2] Ahmed N, Barsoum I, Haidemenopoulos G, et al. Process parameter selection and optimization of laser powder bed fusion for 316L stainless steel: a review. J Manuf Process 2022;75:415–34.
[3] Bartolomeu F, Buciumeanu M, Pinto E, et al. 316L stainless steel mechanical and tribological behavior-A comparison between selective laser melting, hot pressing and conventional casting. Addit Manuf 2017;16:81–9.
[4] Oliveira JP, Santos TG, Miranda RM. Revisiting fundamental welding concepts to improve additive manufacturing: from theory to practice. Prog Mater Sci 2020;107:100590.
[5] Korkmaz ME, Gupta MK, Robak G, et al. Development of lattice structure with selective laser melting process: a state of the art on properties, future trends and challenges. J Manuf Process 2022;81:1040–63.
[6] Bevans B, Ramalho A, Smoqi Z, et al. Monitoring and flaw detection during wire-based directed energy deposition using in-situ acoustic sensing and wavelet graph signal analysis. Mater Des 2023;225:111480.
[7] Felice IO, Shen J, Barragan AFC, et al. Wire and arc additive manufacturing of Fe-based shape memory alloys: microstructure, mechanical and functional behavior. Mater Des 2023;231:112004.
[8] Tan JH, Wong WLE, Dalgarno KW. An overview of powder granulometry on feedstock and part performance in the selective laser melting process. Addit Manuf 2017;18:228–55.
[9] Svetlizky D, Das M, Zheng B, et al. Directed energy deposition (DED) additive manufacturing: physical characteristics, defects, challenges and applications. Mater Today 2021;49:271–95.
[10] Wang D, Zhou C, Filatov AS, et al. Direct synthesis and chemical vapor deposition of 2D carbide and nitride MXenes. Science 2023;379(6638):1242–7.
[11] Casati R, Lemke J, Vedani M. Microstructure and fracture behavior of 316L austenitic stainless steel produced by selective laser melting. J Mater Sci Technol 2016;32(8):738–44.
[12] Larimian T, Kannan M, Grzesiak D, et al. Effect of energy density and scanning strategy on densification, microstructure and mechanical properties of 316L stainless steel processed via selective laser melting. Mater Sci Eng, A 2020;770:138455.
[13] Dutt AK, Bansal GK, Tripathy S, et al. Optimization of selective laser melting (SLM) additive manufacturing process parameters of 316L austenitic stainless steel. Trans Indian Inst Met 2022;76(2):335–45.
[14] Wei Y-p, Yang H, Cheng J-c, et al. Compression behavior of 316L lattice structures produced by indirect additive manufacturing. China Foundry 2023;20(2):83–8.
[15] Rosa F, Manzoni S, Casati R. Damping behavior of 316L lattice structures produced by selective laser melting. Mater Des 2018;160:1010–8.
[16] Xu Z, Guo Y, Liu Y, et al. The martensitic transformation behavior and shape memory effect of laser powder bed fusion NiTi alloys influenced by rare earth addition. Mater Sci Eng, A 2022;848:143350.
[17] Zhang Z, Yang Q, Yu Z, et al. Influence of Y2O3 addition on the microstructure of TiC reinforced Ti-based composite coating prepared by laser cladding. Mater Char 2022;189:111962.
[18] Zhai W, Zhou W, Nai SML. Effect of interface wettability on additively manufactured metal matrix composites: a case study of 316L-Y2O3 oxide dispersion-strengthened steel. Metals 2024;14(2):170.
[19] AlMangour B, Baek M-S, Grzesiak D, et al. Strengthening of stainless steel by titanium carbide addition and grain refinement during selective laser melting. Mater Sci Eng, A 2018;712:812–8.
[20] Zhai W, Zhou W, Nai SML. Grain refinement and strengthening of 316L stainless steel through addition of TiC nanoparticles and selective laser melting. Mater Sci Eng, A 2022;832:142460.
[21] Li J, Qu H, Bai J. Grain boundary engineering during the laser powder bed fusion of TiC/316L stainless steel composites: new mechanism for forming TiC-induced special grain boundaries. Acta Mater 2022;226:117605.
[22] Abedi M, Moskovskikh D, Romanovski V, et al. Unlocking the potential of graphene-reinforced AlSi10Mg nanocomposites in laser powder bed fusion: a comprehensive review. J Alloys Compd 2024;978:173441.
[23] Mandal A, Tiwari JK, AlMangour B, et al. Tribological behavior of graphene-reinforced 316L stainless-steel composite prepared via selective laser melting. Tribol Int 2020;151:106525.
[24] Lenders S, Thoene M, Riemer A, et al. On the mechanical behaviour of titanium alloy TiAl6V4 manufactured by selective laser melting: fatigue resistance and crack growth performance. Int J Fatig 2013;48:300–7.
[25] Liu H, Yang B, Zhang J, et al. Surface mechanical property and residual stress stability of shot-peened Mg-8Gd-3Y alloy by in-situ X-ray diffraction. J Mater Res Technol 2023;26:3015–24.
[26] Shi Y, Wang Y, Li S, et al. Recrystallization texture analysis of FeCoNiCrMnAl0.5 high-entropy alloy investigated by high-energy X-ray diffraction. Metals 2022;12(10):1674.
[27] Takase A, Ishimoto T, Suganuma R, et al. Lattice distortion in selective laser melting (SLM)-manufactured unstable β-type Ti-15Mo-5Zr-3Al alloy analyzed by high-precision X-ray diffractometry. Scripta Mater 2021;201:113953.
[28] Mandal A, Tiwari JK, Sathish N, et al. Microstructural and mechanical properties evaluation of graphene reinforced stainless steel composite produced via selective laser melting. Mater Sci Eng, A 2020;774:138936.
[29] Mandal A, Tiwari JK, AlMangour B, et al. Microstructural and thermal expansion behaviour of graphene reinforced 316L stainless steel matrix composite prepared via powder bed fusion additive manufacturing. Results Mater. 2021;11:100200.
[30] Wang YM, Voisin T, McKeown JT, et al. Additively manufactured hierarchical stainless steels with high strength and ductility. Nat Mater 2017;17(1):63–71.
[31] Tabandeh-Khorshid M, Kumar A, Omrani E, et al. Synthesis, characterization, and properties of graphene reinforced metal-matrix nanocomposites. Compos B Eng 2020;183:107664.
[32] Hu Z, Tong G, Lin D, et al. Graphene-reinforced metal matrix nanocomposites-a review. Mater Sci Technol 2016;32(9):930–53.
[33] Han Y, Zhang Y, Jing H, et al. Selective laser melting of low-content graphene nanoplatelets reinforced 316L austenitic stainless steel matrix: strength enhancement without affecting ductility. Addit Manuf 2020;34:101381.
[34] Xiang S, Wang X, Gupta M, et al. Graphene nanoplatelets induced heterogeneous bimodal structural magnesium matrix composites with enhanced mechanical properties. Sci Rep 2016;6:38824.
[35] Jeon C-H, Jeong Y-H, Seo J-J, et al. Material properties of graphene/aluminum metal matrix composites fabricated by friction stir processing. Int J Precis Eng Manuf 2014;15(6):1235–9.
[36] He Z, Jia N, Yan H, et al. Multi-heterostructure and mechanical properties of N-doped FeMnCoCr high entropy alloy. Int J Plast 2021;139:102965.

[37] Kubin LP, Mortensen A. Geometrically necessary dislocations and strain-gradient plasticity: a few critical issues. Scripta Mater 2003;48(2):119–25.
[38] Lu HZ, Ma HW, Cai WS, et al. Stable tensile recovery strain induced by a Ni4Ti3 nanoprecipitate in a Ni50.4Ti49.6 shape memory alloy fabricated via selective laser melting. Acta Mater 2021;219:117261.
[39] Xu Z, Guo Y, Liu Y, et al. Anti-tribocorrosion resistance of NiTi–CeO2 alloys fabricated by laser powder bed fusion. Compos Commun 2023;38:101512.
[40] Guo Y, Xu Z, Wang Q, et al. Corrosion resistance and biocompatibility of graphene oxide coating on the surface of the additively manufactured NiTi alloy. Prog Org Coating 2022;164:106722.
[41] Guo Y, Yan X, Yang Y, et al. Graphene oxide/hydroxyapatite composite coatings on additively manufactured NiTi alloy for biomedical applications. Ceram Int 2024;50 (1):2479–89.
[42] Shen J, Choi YT, Yang J, et al. Fabrication of spatially-variable heterostructured CoCrFeMnNi high entropy alloy by laser processing. Mater Sci Eng 2024;896: 146272.
[43] Li Z, Ni H, Chen Z, et al. Enhanced tensile properties and corrosion resistance of stainless steel with copper-coated graphene fillers. J Mater Res Technol 2020;9(1): 404–12.
[44] Sprouster DJ, Cunningham WS, Halada GP, et al. Dislocation microstructure and its influence on corrosion behavior in laser additively manufactured 316L stainless steel. Addit Manuf 2021;47:102263.
[45] Sik KY, Lee JH, tae K k, et al. Intergranular corrosion mechanism of slightly-sensitized and UNSM-treated 316L stainless sSteel. Corrosion Sci Technol 2016;15 (5):226–36.
[46] Guo Y, Xu Z, Liu M, et al. The corrosion resistance, biocompatibility and biomineralization of the dicalcium phosphate dihydrate coating on the surface of the additively manufactured NiTi alloy. J Mater Res Technol 2022;17:622–35.
[47] Dong Y, Wang T, Xu Y, et al. A polydopamine-based calcium phosphate/graphene oxide composite coating on magnesium alloy to improve corrosion resistance and biocompatibility for biomedical applications. Materialia 2022;21:101315.
[48] Wang T, Xu Y, Liu Z, et al. A chitosan/polylactic acid composite coating enhancing the corrosion resistance of the bio-degradable magnesium alloy. Prog Org Coating 2023;178:107469.
[49] Li D, Cui X, Wen X, et al. Effect of CeO2 nanoparticles modified graphene oxide on electroless Ni-P coating for Mg-Li alloys. Appl Surf Sci 2022;593:151381.
[50] Hu Y, Cong W, Wang X, et al. Laser deposition-additive manufacturing of TiB-Ti composites with novel three-dimensional quasi-continuous network microstructure: effects on strengthening and toughening. Compos B Eng 2018;133: 91–100.
[51] Yang Y, Yang M, He C, et al. Rare earth improves strength and creep resistance of additively manufactured Zn implants. Compos B Eng 2021;216:108882.
[52] Guo Y, Xu Z, Liu Y, et al. Achieving illustrious friction and corrosion resistance on a laser powder bed fusion nitinol rare earth alloy. Mater Today Adv 2023;17: 100350.
[53] Zhang L, Zhai W, Zhou W, et al. Improvement of mechanical properties through inhibition of oxidation by adding TiC particles in laser aided additive manufacturing of stainless steel 316L. Mater Sci Eng, A 2022;853:143767.
[54] Rajkumar K, Aravindan S. Tribological behavior of microwave processed copper-nanographite composites. Tribol Int 2013;57:282–96.
[55] Moghadam AD, Omrani E, Menezes PL, et al. Mechanical and tribological properties of self-lubricating metal matrix nanocomposites reinforced by carbon nanotubes (CNTs) and graphene-areview. Compos B Eng 2015;77:402–20.
[56] Fattahi M, Gholami AR, Eynalvandpour A, et al. Improved microstructure and mechanical properties in gas tungsten arc welded aluminum joints by using graphene nanosheets/aluminum composite filler wires. Micron 2014;64:20–7.
[57] Lahiri D, Bakshi SR, Keshri AK, et al. Dual strengthening mechanisms induced by carbon nanotubes in roll bonded aluminum composites. Mater Sci Eng 2009;523 (1–2):263–70.